



**University of  
Zurich**<sup>UZH</sup>

**Zurich Open Repository and  
Archive**

University of Zurich  
Main Library  
Strickhofstrasse 39  
CH-8057 Zurich  
[www.zora.uzh.ch](http://www.zora.uzh.ch)

---

Year: 2015

---

## **Diffusion MRI with concurrent magnetic field monitoring**

Wilm, Bertram J ; Nagy, Zoltan ; Barmet, Christoph ; Vannesjo, S Johanna ; Kasper, Lars ; Haeblerlin, Max ; Gross, Simon ; Dietrich, Benjamin E ; Brunner, David O ; Schmid, Thomas ; Pruessmann, Klaas P

**Abstract:** **PURPOSE:** Diffusion MRI is compromised by unknown field perturbation during image encoding. The purpose of this study was to address this problem using the recently described approach of concurrent magnetic field monitoring. **METHODS:** Magnetic field dynamics were monitored during the echo planar imaging readout of a common diffusion-weighted MRI sequence using an integrated magnetic field camera setup. The image encoding including encoding changes over the duration of entire scans were quantified and analyzed. Field perturbations were corrected by accounting for them in generalized image reconstruction. The impact on image quality along with geometrical congruence among different diffusion-weighted images was assessed both qualitatively and quantitatively. **RESULTS:** The most significant field perturbations were found to be related to higher-order eddy currents from diffusion-weighting gradients and B0 field drift as well as gradual changes of short-term eddy current behavior and mechanical oscillations during the scan. All artifacts relating to dynamic field perturbations were eliminated by incorporating the measured encoding in image reconstruction. **CONCLUSION:** Concurrent field monitoring combined with generalized reconstruction enhances depiction fidelity in diffusion imaging. In addition to artifact reduction, it improves geometric congruence and thus facilitates image combination for quantitative diffusion analysis.

DOI: <https://doi.org/10.1002/mrm.25827>

Posted at the Zurich Open Repository and Archive, University of Zurich

ZORA URL: <https://doi.org/10.5167/uzh-114480>

Journal Article

Accepted Version

Originally published at:

Wilm, Bertram J; Nagy, Zoltan; Barmet, Christoph; Vannesjo, S Johanna; Kasper, Lars; Haeblerlin, Max; Gross, Simon; Dietrich, Benjamin E; Brunner, David O; Schmid, Thomas; Pruessmann, Klaas P (2015). Diffusion MRI with concurrent magnetic field monitoring. *Magnetic Resonance in Medicine*, 74(4):925-933.

DOI: <https://doi.org/10.1002/mrm.25827>

# Diffusion MRI with concurrent magnetic field monitoring

Bertram J Wilm<sup>1</sup>, Zoltan Nagy<sup>2</sup>, Christoph Barmet<sup>1,3</sup>, S Johanna Vannesjo<sup>1</sup>, Lars Kasper<sup>1,4</sup>, Max Haeberlin<sup>1</sup>,  
Simon Gross<sup>1</sup>, Benjamin E Dietrich<sup>1</sup>, David O Brunner<sup>1</sup>, Thomas Schmid<sup>1</sup> and Klaas P Pruessmann<sup>1</sup>

*1: Institute for Biomedical Engineering, University of Zurich and ETH Zurich, Switzerland*

*2: Laboratory for Social and Neural Systems Research, University of Zurich, Switzerland*

*3: Skope Magnetic Resonance Technologies LCC, Zurich, Switzerland*

*4: Translational Neuromodeling Unit, Institute for Biomedical Engineering, University of Zurich and ETH  
Zurich, Switzerland*

Mailing Address: Bertram J. Wilm  
Institute for Biomedical Engineering  
University and ETH Zurich  
Gloriastrasse 35  
CH-8092 Zurich, Switzerland  
Tel.: +41-44-632 82 36  
Fax: +41-44-632 11 93  
Email: [wilm@biomed.ee.ethz.ch](mailto:wilm@biomed.ee.ethz.ch)

Type: Rapid Communication

Running title: Diffusion MRI with concurrent magnetic field monitoring

Word count: ca. 3400

## **Abstract**

*Purpose: Diffusion MR imaging is compromised by unknown field perturbation during image encoding. The purpose of this work is to explore the potential of addressing this problem by the recent approach of concurrent magnetic field monitoring.*

*Methods: Magnetic field dynamics were monitored during the EPI readout of a common diffusion-weighted MRI sequence using an integrated magnetic field camera setup. The image encoding including encoding changes over the duration of entire scans were quantified and analyzed. Field perturbations were corrected by accounting for them in generalized image reconstruction. The impact on image quality along with geometrical congruence among differently diffusion-weighted images was assessed both qualitatively and quantitatively.*

*Results: The most significant field perturbations were found to be related to higher-order eddy currents from diffusion-weighting gradients,  $B_0$  field drift, as well as gradual changes of short-term eddy current behavior and mechanical oscillations during the scan. All artifacts relating to dynamic field perturbations were eliminated by incorporating the measured encoding in image reconstruction.*

*Conclusion: Concurrent field monitoring combined with generalized reconstruction enhances depiction fidelity in diffusion imaging. In addition to artifact reduction it improves geometric congruence and thus facilitates image combination for quantitative diffusion analysis.*

## Introduction

Diffusion-weighted (DW) MR (1) imaging (2) allows for a non-invasive assessment of water diffusion and thereby enables probing of the tissue microstructure. DW imaging (DWI) is a standard method for the early detection of stroke (3), and the structural information from DW MR data has gained increasing interest in clinical practice and research in the past years.

Diffusion MRI is challenging in many respects and various MR sequences have been suggested to achieve optimal image quality. One fundamental challenge is the inherently low signal-to-noise-ratio (SNR) of DW images, which motivates the use of MR sequences with high SNR efficiency. Another challenge is the sensitivity to motion such as stemming from breathing and cardiac pulsation. In conjunction with the strong diffusion sensitizing gradients, motion results in unpredictable phase changes as well as echo-time shifts for each acquisition. This impedes the application of multi-shot acquisition techniques (4) or fast-spin-echo sequences (5). In recent years these problems have been addressed and promising results have been shown in particular by using multi-shot DWI approaches that estimate motion-related phase errors by k-space oversampling (6) or using navigators (7–9). Nevertheless, owing to their inherent robustness against motion, the vast majority of scans that are performed in practice are single-shot echo-planar imaging (EPI) sequences (10).

However, single-shot EPI is susceptible to several artifacts including global and local image distortions as well as image ghosts, which can impair the clinical value of obtained DW images and drastically limit the accuracy of quantitative diffusion (11)(12) imaging. The latter requires the combination of DW images to fit a chosen diffusion model, which increases the sensitivity to encoding perturbations that result in geometrical incongruence among variably diffusion-encoded images.

One problem common to all EPI acquisition strategies is their sensitivity to gradient system imperfections. In particular, gradient delays and eddy currents cause inconsistency among the acquired k-space lines with different read direction and thus result in half-FOV ghosting artifacts. On most clinical MRI systems this problem is addressed by EPI phase correction techniques (13). However, EPI phase correction does not account for all gradient imperfections. Moreover, gradient heating can render such calibrations invalid by altering the behavior of short-term eddy currents and mechanical oscillations.

A second challenge are eddy current field effects that are induced by the diffusion-sensitizing gradients. Since the duration of the diffusion encoding gradients is long, the resulting eddy current fields with long time constants can significantly perturb the subsequent image encoding. In the images, these effects result in distortions as well as ghosting artifacts that vary with the applied DW gradients. Eddy currents are diminished by the MR system's eddy current compensation (ECC), i.e., pre-emphasis of the demand waveform that is sent to the gradient amplifier as well as demodulation of  $B_0$  eddy currents. Another approach is to reduce eddy current effects by sequence design, for instance with bipolar diffusion gradient lobes (14) or twice-refocused spin-echo sequences (15,16). Remaining eddy currents are typically addressed by co-registration after image reconstruction (17)(18)(19). However, image co-registration only addresses geometric distortions and commonly assumes an affine transformation model, which can be insufficient to model the actual image distortions. Moreover, co-registration requires sufficient SNR, which is often not available, particularly with strong diffusion encoding (high b-values / q-values).

Another source of image artifacts are drifts of the static  $B_0$  field. Such field changes can be caused by temperature changes of the MR system's hardware components such as the shim irons or the heat shield. When the field changes are of 0<sup>th</sup> order they result in image shifts as well as minor ghosting artifacts. Field drifts of 1<sup>st</sup> order in space result in image scaling and shearing. Except for  $B_0$ -induced ghosts, field drifts up to the 1<sup>st</sup> order can potentially be addressed by the above-mentioned image co-registration methods, again having to rely on high SNR in individual images. Field drifts of higher spatial order must be addressed at the image reconstruction level, e.g., by static  $B_0$  off-resonance correction (20)(21)(22). Such approaches, however, can only be applied when knowledge of these field changes is available.

In this work, we explore the potential of addressing field imperfections in diffusion imaging comprehensively by the recent concept of concurrent magnetic field monitoring (23–25). Field monitoring yields the actual spatiotemporal evolution of the magnetic field during image acquisition. Thus it jointly captures eddy current effects, temperature-related field drifts and changing behavior of the gradient system, as well as dynamic field changes of external origin. Full use of this information at the reconstruction level requires generalization of the traditional Fourier perspective such as to account for higher-order spatial encoding. A suitable algebraic strategy for this purpose was recently proposed and shown to be effective at addressing eddy currents due to diffusion gradients (26). We now seek to evaluate the prospect of this approach from the perspective of diffusion imaging practice. To this end, we assess its benefits for typically used single-shot DW EPI sequences with a high-performing gradient system in a phantom and in vivo. Furthermore, we study the ability to compensate for thermal system drifts and imperfect gradient calibration.

## **Methods**

### **Acquisition Setup**

All scans were performed on a 3T Achieva System (Philips Healthcare, Best, The Netherlands) using an 8-element head receive coil array. Sixteen transmit/receive  $^{19}\text{F}$ -based NMR probes were mounted on the surface of the head array (Fig.1). The probe positions were chosen such as to achieve optimal conditioning for expansion into a 3<sup>rd</sup>-order spherical harmonic field model. This was achieved by placing the probes in 4 rings with 5-6-4-1 probes per ring respectively (27). The coordinates of the probes are provided in the appendix of this document.

Probe excitation was triggered by the physiology trigger of the MR systems (TTL signal); a dedicated RF transmit chain was used to excite the field probes (28). The field probes'  $^{19}\text{F}$  signals were amplified and then digitized by the MR system's spectrometer, together with the eight  $^1\text{H}$  signals from the head-coil array. The spectrometer was programmed to perform multiple-channel acquisition for both nuclei.

In-vitro experiments were performed on a spherical phantom filled with low-diffusivity silicon oil (AK 500, Wacker Chemie AG, Munich, Germany) to minimize signal attenuation by diffusion weighting. In-vivo experiments were performed on a healthy subject (female, 22 years) after written informed consent and in accordance with local ethics regulations.

## **MR Sequence Parameters**

Single-shot DW-EPI scans were acquired with a FOV of  $(230 \text{ mm})^2$  and an in-plane resolution of  $(2.0 \text{ mm})^2$  in the phantom and  $(1.7 \text{ mm})^2$  in-vivo in one transverse slice (thickness = 2 mm). Stejskal-Tanner (single-refocused) diffusion weighting was applied in 6 non-coplanar orientations  $((-2/3, -2/3, -1/3)^T (-1/3, 2/3, -2/3)^T (-2/3, 1/3, 2/3)^T (-2^{0.5}/2, 0, -2^{0.5}/2)^T (-2^{0.5}/2, 2^{0.5}/2, 0)^T$  and  $(0, 2^{0.5}/2, 2^{0.5}/2)^T$ ) with  $b = 1000 \text{ s/mm}^2$ . In addition a  $b_0$  ( $b = 0 \text{ s/mm}^2$ ) reference image was acquired to obtain a full DTI dataset. SENSE undersampling by a factor of 3 was used to reduce sensitivity to  $B_0$  off-resonance distortions and  $T_2^*$  blurring. This was implemented by performing an interleaved-EPI sequence with 3 interleaves, which were each treated separately as a single-shot acquisition in the reconstruction. The gradient mode was set to maximum gradient strength to allow for short echo times (TE). TE was 60.3 ms (in vitro) and 69.1 ms (in vivo) with a readout duration of 32 ms (bandwidth = 31.2 Hz per pixel) and 41.5 ms (bandwidth = 24.1 Hz per pixel) respectively. In vitro, two static saturation slabs were applied perpendicular to the slice to add some structure to the phantom. The number of averages was set to 9 for the in-vitro scans and 27 in the in-vivo scans. To allow for studying temperature-related field effects separately, gradient heating of the DW scan itself was minimized by imaging only a single slice and choosing a long repetition time (TR = 5s).

In addition two standard spin-warp gradient-echo data sets (resolution:  $2.0 \times 2.0 \text{ mm}^2$ , slice thickness: 4 mm, TE: 3.6 and 3.9 ms) were acquired and used to calculate coil sensitivity and static  $\Delta B_0$  maps.

For all scans, the encoding fields were recorded using the field probes simultaneously with image acquisition. For the gradient echo scans, the field probes were excited after slice selection. In the DW scans the field probes were excited after the diffusion-encoding gradients, since the large gradient lobes would otherwise fully dephase the field probe signal. From the probe data, a 3<sup>rd</sup>-order phase model, including the 1<sup>st</sup>-order k-space trajectory, was calculated by spherical-harmonic expansion (26) with concomitant-field correction (29).

## **Specific experiments**

In the phantom, three DW experiments were performed.

In *experiment 1*, the DW sequence was played out as described in the previous section. The dataset was acquired to evaluate the effect of the DW gradients on the encoding and the resulting images.

In *experiment 2*, the above DW scan was repeated with the MR system's eddy current correction (ECC) turned off to mimick a miscalibrated or otherwise less refined gradient system.

In *experiment 3*, experiment 1 was repeated after a gradient-intensive EPI-based fMRI scan with a duration of 12 minutes that was known to heat up the MR system, to evaluate the effect of the changing MR system temperature on gradient and field drifts during a scan. The image averages were acquired in the outer loop (dynamics) of the scan such that the same contrasts were acquired in different temperature states.

In vivo, experiment 3 was repeated.

## **Field encoding visualization**

The unit of the phase coefficients is  $\text{rad}/\text{m}^N$  for basis functions of degree  $N = 0,1,2,3$ . Due to different spatial features and scaling factors the coefficients per se are difficult to interpret and compare. Therefore, the phase coefficients are visualized by plotting the related maximum field excursion, in radians ( $\text{rad}_{\text{max}}$ ), in a centered sphere of 20 cm diameter. To study the effects of the DW gradients, the phase evolution during the DW experiments was plotted after subtraction from the  $b_0$  scan's phase coefficients. This was done for the scans with (experiment 1) and without (experiment 2) the MR system's ECC for the first two diffusion directions. To study temperature-related field effects (experiment 3), the phase evolution of the first average of the  $b_0$  and the first two DW scans were plotted after subtraction of the relating last average that was acquired approx. 5 minutes later.

### **Image Reconstruction**

All DWI datasets were reconstructed using iterative image reconstruction incorporating higher-order fields as well as coil sensitivity and  $\Delta B_0$  maps (26). The gradient echo images yielding sensitivity and  $\Delta B_0$  maps were reconstructed with the same algorithm and likewise on the basis of concurrent monitoring.

To evaluate the effect of field contributions relating to the DW gradients, the DTI data from the experiments with ECC (experiment 1) was reconstructed in four different ways. First, assuming perfect gradient behavior, based on the *nominal* trajectory without any correction. Second, using the 0<sup>th</sup>- and 1<sup>st</sup>-order monitored trajectory from the  $b_0$  scan (*monitored  $b_0$* ), but neglecting higher-order fields and DW eddy currents. Third, using the 0<sup>th</sup>- and 1<sup>st</sup>-order monitored trajectory from concurrently monitored fields relating to each acquisition, to assess the remaining effect of higher-order fields. Fourth, using the concurrently monitored full 3<sup>rd</sup>-order phase expansions relating to each acquisition (*3<sup>rd</sup>-order monitored*). To assess geometric consistency, a relative difference image between the DW and  $b_0$  images was calculated for each of the DW images in each of the image sets.

The relative difference between two magnitude images  $I_1$  and  $I_2$  was calculated as  $2(I_1 - I_2)/(I_1 + I_2)$  for each voxel and was displayed using either a  $\pm 10\%$  or a  $\pm 100\%$  scale. The relative difference was set to zero where  $(I_1 + I_2)$  was below a threshold near the image noise level.

For the non-ECC scans (experiment 2), reconstruction and evaluation were performed similarly, but omitting the *nominal* reconstructions.

To assess the effect of gradient and field drift during the scan (experiment 3), all images were reconstructed using the monitored trajectory of the first average relating to each DW direction. The same reconstruction was then repeated taking measured individual  $B_0$  shifts into account. A third set of images was reconstructed using the individually monitored 3<sup>rd</sup>-order phase expansions. Geometrical congruence and image quality were assessed by subtracting the first two sets from the individually 3<sup>rd</sup>-order monitored reconstructions. In addition, congruence between the DW images and the  $b_0$  image was assessed for all reconstructed datasets.

For the in-vivo DTI dataset, image reconstruction based on the *nominal*, *monitored  $b_0$*  (0<sup>th</sup> and 1<sup>st</sup>-order) and *individual 3<sup>rd</sup>-order* monitored trajectories was performed. Subsequently, the mean DW image, an apparent diffusion coefficient (ADC) map, a fractional anisotropy (FA) map and the color-coded FA (cFA) map were calculated for all image sets without image co-registration.

## Results

### Observed field encoding

In the scans with ECC (experiment 1), the dominant phase terms during the  $b_0$  acquisition (Fig.2a) were the regular 1st-order (k-space) terms reflecting the EPI readout with only minor ( $< 0.5 \text{ rad}_{\text{max}}$ ) contribution from higher-order terms. In addition an approximately constant  $B_0$  offset (linear 0<sup>th</sup>-order phase) was present. When adding the DW gradients (Fig.2b-c), additional 0<sup>th</sup> order deviations up to  $3.5 \text{ rad}$  as well as higher-order terms up to  $3.5 \text{ rad}_{\text{max}}$  (2<sup>nd</sup> order) and  $1.3 \text{ rad}_{\text{max}}$  (3<sup>rd</sup> order) were observed. The time courses of the higher-order terms indicate underlying eddy currents with noticeable decay during the readout. In the scans without ECC (experiment 2) (Fig.2d-f), the apparent higher-order field terms were very similar to those with ECC (Fig.2a-c) as should be expected. However, the absence of the MR system's 0<sup>th</sup>- and 1<sup>st</sup>-order ECC resulted in strong deviations in the 0<sup>th</sup>-order ( $20 \text{ rad}$ ) and 1<sup>st</sup>-order ( $50 \text{ rad}_{\text{max}}$ ) terms. Heating-related changes (experiment 3) (Fig.2g-i) were predominantly of 0<sup>th</sup>-order and consistent with slow  $B_0$  change. Smaller differences were observed in the 1<sup>st</sup>-order terms, particularly for the direction of the read gradient. Only minor higher-order drift was observed. The drift was very similar for the  $b_0$  (Fig.2g) and the DW images (Fig.2h,i).

### Image reconstruction

For the scans with ECC (experiment 1), image reconstruction based on the nominal trajectory resulted in substantial ghosting artifacts (Fig.3a) as well as image incongruence that were clearly apparent on both the full-scale and the 10% scale difference images (Fig.3b). Reconstruction based on field monitoring during the  $b_0$  scan (Fig.3c) largely removed ghosting and improved the congruence among the images. However, the difference images (Fig.3d) still indicate significant geometric inconsistency. The differences of up to 100% at the phantom edges indicate relative distortions in the order of  $2/3$  of a voxel size. The reconstructions using the concurrently monitored 0<sup>th</sup>- and 1<sup>st</sup>-order terms showed similar ghosting and distortion levels (Fig.3e,f). Incorporation of higher-order terms (Fig.3g) resulted in virtually exact geometrical congruence and also reduced ghosting below the level of visibility (Fig.3h).

For the data set without ECC (experiment 2), image reconstruction based on monitoring of the  $b_0$  scan resulted in strong relative distortion of the different DW images (Fig.4a) and thus unacceptable variability among the DW and  $b_0$  images (Fig.4b). 3<sup>rd</sup>-order reconstruction based on concurrently monitored field evolutions (Fig.4c) still yielded near-perfect ghost correction and image congruence (Fig.4d). Merely an intensity difference among the DW and  $b_0$  images and subtle geometrical inconsistency remained apparent (Fig.4d).

The analysis of the effect of temperature drift during the scan showed that neglecting temperature-related encoding errors caused prominent ghosting artifacts (Fig.5a) as well as shifting of the image by several pixels in the phase encoding direction (Fig.5b). Correcting for the individual  $B_0$  drifts (Fig.5d) removed most of the image shifts (Fig.5e), however prominent image ghosting remained (Fig. 5e). In both cases, the relative differences to the corresponding  $b_0$  scans showed that artifacts levels also varied slightly depending on the diffusion encoding (Fig.5c,f). Ghost-free images with matching geometry were obtained when reconstructing all images based on individual concurrent monitoring (Fig.5g,h) indicating that these images represent the phantom faithfully.



In the in-vivo dataset, reconstruction based on the nominal trajectory (Fig.6a) resulted in visible ghosting artifacts, which were particularly noticeable in the  $b_0$  images and the ADC map. In addition, the FA maps appeared noisy and the cFA images showed non-anatomical diffusion anisotropy throughout the brain, probably resulting from the geometrical mismatch of the DW images. Using the k-space trajectory measured during the  $b_0$  scan (Fig.6b) slightly improved the results, but artifacts were still apparent. Incorporation of the monitored higher-order field effects (Fig.6c) resulted in the removal of any visible ghosts and the non-anatomical anisotropy.

## Discussion

In this study, the most significant field perturbations in DWI acquisitions have been found to relate to eddy currents induced by the diffusion weighting gradients,  $B_0$  drift, gradual changes of the short term gradient system response during the scan. It has been demonstrated that these perturbations can be comprehensively addressed by concurrent field monitoring and algebraic image reconstruction, yielding virtually artifact-free geometrically congruent image data.

Eddy current effects caused by DW gradients had significant higher-order components not amenable to ECC. Only by higher-order reconstruction it was possible to account for the full range of field distortions. The commonly employed registration methods based on affine transformations (19) implicitly assume spatially linear and temporally constant eddy current fields. According to the findings of this work neither of these assumptions typically holds for DWI and thus only incomplete co-registration can be expected with affine models. Another disadvantage of image co-registration is its dependence on sufficient image SNR. This is particularly problematic for high b-value and q-space data. Distortion models with more degrees of freedom have been explored (30), yet arguably require even more SNR to achieve stable results. The eddy current effects observed in the present study remained largely unchanged by gradient heating and generally proved very reproducible. Therefore, image reconstruction based on prior calibration of DW eddy currents, e.g. using gradient impulse response measurements (31), may well be possible. Fast implementations of higher-order reconstruction (32), which are well suited to correct for eddy currents in DWI, may then be used to make the correction practical for clinical applications. Alternatively image reconstruction may be accelerated by using dedicated computing hardware (33).

Slow 0<sup>th</sup>-order drifts as well as changes in high frequency 1<sup>st</sup>-order fields during the scan (experiment 3) following gradient intensive scanning probably related to temperature changes in different components of the MR system. The analysis of the phase evolutions showed that mere correction of the slow  $B_0$  changes was insufficient to address all artifacts in the images. The remaining ghosting artifacts could be attributed to changes in the high-frequency 1<sup>st</sup>-order encoding following gradient action, which probably relate to changes in gradient eddy currents or mechanical vibrations (34). Similar ghosting artifacts can be expected for non-monitored scans when using pre-scan EPI phase calibration (13) during or after gradient intensive scans. Phase reference scans, embedded in the actual EPI readout (35), can partially address this problem, but also prolong echo times.

By turning off the MR system's ECC (experiment 2), a miscalibrated or otherwise less refined gradient system was simulated. Even in this case, field monitoring and algebraic reconstruction achieved virtually

complete ghost suppression and image congruence well below the pixel scale. Thus, the presented method may relax specification requirements on MR system/gradient hardware and its calibration. The remaining issues in this experiment were differences in image magnitude and minor residual misalignment between images with the different DW directions. They are likely related to through-plane dephasing by eddy-current gradient field in the slice direction and slight slice shifts due to strong  $B_0$  eddy currents, respectively. The issue could be further addressed by modelling and correcting for this effect.

Similarly, concurrent field monitoring removed any visible ghosting artifacts in the in-vivo DW images. Moreover, the results indicate that the achieved geometrical congruence strongly improves the quality of quantitative diffusion data in-vivo, which was demonstrated by the removal of non-anatomical diffusion tensor anisotropy throughout the brain. Field monitoring also captures breathing related field changes in head imaging as has been recently reported (36), which probably also contributed to the achieved geometrical consistency in vivo.

Enhanced depiction accuracy and geometrical congruence hold promise for many diffusion studies. These include q-space diffusion models (12)(37), investigations into the microstructure of grey matter (38,39), as well as any application that aims to investigate diffusion in the brain at high resolution (40,41).

Notably, concurrent field monitoring also improves the accuracy of parametric maps (e.g. receive coil sensitivities or off-resonance maps) and their geometric consistency with data to be reconstructed with their help. Such consistency is key to the accuracy of signal models, which in turn is the basis of faithful reconstruction. Therefore concurrent field monitoring may also prove valuable for other DWI strategies, e.g. with multiple-shot acquisition (6,9) or more complex encoding models including joint estimation of parametric data (42).

## Appendix

The field probe's positions are denoted relative to the iso-center in the non-angulated coordinate system (left-right, anterior-posterior, head-feet)<sup>T</sup> in meters:

$(0.0512, -0.1043, 0.0844)^T, (-0.0820, 0.0324, -0.0908)^T, (-0.0378, 0.1075, -0.0015)^T, (0.1206, -0.0352, -0.0012)^T,$   
 $(-0.0528, -0.0671, -0.0952)^T, (0.0024, 0.0904, -0.0935)^T, (0.1090, 0.0447, 0.0829)^T, (0.0921, 0.0317, -0.0947)^T,$   
 $(-0.1004, -0.0458, 0.0823)^T, (-0.0853, -0.0710, 0.0014)^T, (0.0007, 0.0022, -0.1547)^T, (0.0228, -0.1116, 0.0052)^T,$   
 $(0.0593, -0.0684, -0.0951)^T, (-0.0415, 0.1041, 0.0860)^T, (0.0817, 0.0848, 0.0004)^T, (-0.1071, 0.0267, 0.0050)^T$

## Bibliography

- (1) Carr HY, Purcell EM. Effects of Diffusion on Free Precession in Nuclear Magnetic Resonance Experiments. *Phys. Rev.* 1954;94:630–638.
- (2) Le Bihan D, Breton E, Lallemand D, Grenier P, Cabanis E, Laval-Jeantet M. MR Imaging of Intravoxel Incoherent Motions: Application to Diffusion and Perfusion in Neurologic Disorders. *Radiology* 1986;161:401–407.
- (3) Moseley ME, Cohen Y, Mintorovitch J, Chileuitt L, Shimizu H, Kucharczyk J, Wendland MF, Weinstein PR. Early Detection of Regional Cerebral Ischemia in Cats:

Comparison of Diffusion- and T2-Weighted MRI and Spectroscopy. *Magn Reson Med* 1990;14:330–346.

- (4) Pipe JG, Farthing VG, Forbes KP. Multishot Diffusion-Weighted FSE Using PROPELLER MRI. *Magn. Reson. Med.* 2002;47:42–52.
- (5) Bastin ME, Le Roux P. On the Application of a Non-CPMG Single-Shot Fast Spin-Echo Sequence to Diffusion Tensor MRI of the Human Brain. *Magn. Reson. Med.* 2002;48:6–14.
- (6) Wang F-N, Huang T-Y, Lin F-H, Chuang T-C, Chen N-K, Chung H-W, Chen C-Y, Kwong KK. PROPELLER EPI: An MRI Technique Suitable for Diffusion Tensor Imaging at High Field Strength with Reduced Geometric Distortions. *Magn Reson Med* 2005;54:1232–1240.
- (7) Golay X, Jiang H, van Zijl PCM, Mori S. High-Resolution Isotropic 3D Diffusion Tensor Imaging of the Human Brain. *Magn Reson Med* 2002;47:837–843.
- (8) Karampinos DC, Van AT, Olivero WC, Georgiadis JG, Sutton BP. High-Resolution Diffusion Tensor Imaging of the Human Pons with a Reduced Field-of-View, Multishot, Variable-Density, Spiral Acquisition at 3 T. *Magn. Reson. Med.* 2009;62:1007–1016.
- (9) Engström M, Skare S. Diffusion-Weighted 3D Multislab Echo Planar Imaging for High Signal-to-Noise Ratio Efficiency and Isotropic Image Resolution. *Magn. Reson. Med* 2013;70:1507–1514.
- (10) Jones DK. *Diffusion MRI: Theory, Methods, and Applications* Oxford University Press 2010. p 784.
- (11) Basser PJ, Pierpaoli C. Microstructural and Physiological Features of Tissues Elucidated by Quantitative-Diffusion-Tensor MRI. 1996. *J. Magn. Reson.* 2011;213:560–570.
- (12) Callaghan T late PT. *Principles of Nuclear Magnetic Resonance Microscopy* Clarendon Press 1993. p 510.
- (13) Bruder H, Fischer H, Reinfelder HE, Schmitt F. Image Reconstruction for Echo Planar Imaging with Nonequidistant K-Space Sampling. *Magn Reson Med* 1992;23:311–323.
- (14) Alexander AL, Tsuruda JS, Parker DL. Elimination of Eddy Current Artifacts in Diffusion-Weighted Echo-Planar Images: The Use of Bipolar Gradients. *Magn Reson Med* 1997;38:1016–1021.
- (15) Reese TG, Heid O, Weisskoff RM, Wedeen VJ. Reduction of Eddy-Current-Induced Distortion in Diffusion MRI Using a Twice-Refocused Spin Echo. *Magn Reson Med* 2003;49:177–182.
- (16) Finsterbusch J. Double-Spin-Echo Diffusion Weighting with a Modified Eddy Current Adjustment. *Magn Reson Imaging* 2010;28:434–440.

- (17) Jezzard P, Barnett AS, Pierpaoli C. Characterization of and Correction for Eddy Current Artifacts in Echo Planar Diffusion Imaging. *Magn. Reson. Med.* 1998;39:801–812.
- (18) Alexander DC, Pierpaoli C, Basser PJ, Gee JC. Spatial Transformations of Diffusion Tensor Magnetic Resonance Images. *IEEE Transactions on Medical Imaging* 2001;20:1131–1139.
- (19) Netsch T, Muiswinkel A van. in *Biomedical Image Registration* (Eds.: JC Gee, JBA Maintz, MW Vannier), Springer Berlin Heidelberg, 2003, pp. 171–180.
- (20) Noll DC, Meyer CH, Pauly JM, Nishimura DG, Macovski A. A Homogeneity Correction Method for Magnetic Resonance Imaging with Time-Varying Gradients. *IEEE Trans Med Imaging* 1991;10:629–637.
- (21) Noll DC, Pauly JM, Meyer CH, Nishimura DG, Macovski A. Deblurring for Non-2D Fourier Transform Magnetic Resonance Imaging. *Magn Reson Med* 1992;25:319–333.
- (22) Sutton BP, Noll DC, Fessler JA. Fast, Iterative Image Reconstruction for MRI in the Presence of Field Inhomogeneities. *IEEE Trans Med Imaging* 2003;22:178–188.
- (23) Barmet C, De Zanche N, Pruessmann KP. Spatiotemporal Magnetic Field Monitoring for MR. *Magn Reson Med* 2008;60:187–197.
- (24) Barmet C, De Zanche N, Wilm BJ, Pruessmann KP. A Transmit/receive System for Magnetic Field Monitoring of in Vivo MRI. *Magn Reson Med* 2009;62:269–276.
- (25) De Zanche N, Barmet C, Nordmeyer-Massner JA, Pruessmann KP. NMR Probes for Measuring Magnetic Fields and Field Dynamics in MR Systems. *Magn Reson Med* 2008;60:176–186.
- (26) Wilm BJ, Barmet C, Pavan M, Pruessmann KP. Higher Order Reconstruction for MRI in the Presence of Spatiotemporal Field Perturbations. *Magn Reson Med* 2011;65:1690–1701.
- (27) Barmet C, Wilm BJ, Pavan M, Katsikatsos G, Keupp J, Mens G, Pruessmann KP. Concurrent Higher-Order Field Monitoring for Routine Head MRI: An Integrated Heteronuclear Setup. In *Proceedings of 20th Annual Meeting of ISMRM*, Stockholm, Sweden, 2010 n.d.:216.
- (28) Dietrich BE, Brunner DO, Wilm BJ, Barmet C, Gross S, Kasper L, Haeberlin M, Schmid T, Vannesjo SJ, Pruessmann KP. A Field Camera for MR Sequence Monitoring and System Analysis. *Magn. Reson. Med.* 2015, DOI: 10.1002/mrm.25770
- (29) Bernstein MA, Zhou XJ, Polzin JA, King KF, Ganin A, Pelc NJ, Glover GH. Concomitant Gradient Terms in Phase Contrast MR: Analysis and Correction. *Magn Reson Med* 1998;39:300–308.
- (30) Andersson JLR, Skare S. A Model-Based Method for Retrospective Correction of Geometric Distortions in Diffusion-Weighted EPI. *Neuroimage* 2002;16:177–199.

- (31) Vannesjo SJ, Haeberlin M, Kasper L, Pavan M, Wilm BJ, Barmet C, Pruessmann KP. Gradient System Characterization by Impulse Response Measurements with a Dynamic Field Camera. *Magn Reson Med* 2013;69:583–593.
- (32) Wilm BJ, Barmet C, Pruessmann KP. Fast Higher-Order MR Image Reconstruction Using Singular-Vector Separation. *IEEE Trans Med Imaging* 2012;31:1396–1403.
- (33) Stone SS, Haldar JP, Tsao SC, Hwu W -m. W, Sutton BP, Liang Z-P. Accelerating Advanced MRI Reconstructions on GPUs. *J Parallel Distrib Comput* 2008;68:1307–1318.
- (34) Busch J, Vannesjo SJ, Barmet C, Pruessmann KP, Kozerke S. Analysis of Temperature Dependence of Background Phase Errors in Phase-Contrast Cardiovascular Magnetic Resonance. *J Cardiovasc Magn Reson* 2014;16,DOI10.1186/s12968-014-0097-6.
- (35) A. Jesmanowicz, Wong, E. E., Hyde, J. S. Phase Correction for EPI Using Internal Reference Lines. *Proc., SMRM, 12th Annual Meeting, New York, 1993 n.d.:1239.*
- (36) Vannesjo SJ, Wilm BJ, Duerst Y, Gross S, Brunner DO, Dietrich BE, Schmid T, Barmet C, Pruessmann KP. Retrospective Correction of Physiological Field Fluctuations in High-Field Brain MRI Using Concurrent Field Monitoring. *Magn Reson Med* 2014,DOI10.1002/mrm.25303.
- (37) Tuch DS, Reese TG, Wiegell MR, Makris N, Belliveau JW, Wedeen VJ. High Angular Resolution Diffusion Imaging Reveals Intravoxel White Matter Fiber Heterogeneity. *Magnetic Resonance in Medicine* 2002;48:577–582.
- (38) Nagy Z, Alexander DC, Thomas DL, Weiskopf N, Sereno MI. Using High Angular Resolution Diffusion Imaging Data to Discriminate Cortical Regions. *PLoS ONE* 2013;8:e63842.
- (39) Aggarwal M, Nauen DW, Troncoso JC, Mori S. Probing Region-Specific Microstructure of Human Cortical Areas Using High Angular and Spatial Resolution Diffusion MRI. *NeuroImage* 2015;105:198–207.
- (40) Miller KL, Stagg CJ, Douaud G, Jbabdi S, Smith SM, Behrens TEJ, Jenkinson M, Chance SA, Esiri MM, Voets NL, Jenkinson N, Aziz TZ, Turner MR, Johansen-Berg H, McNab JA. Diffusion Imaging of Whole, Post-Mortem Human Brains on a Clinical MRI Scanner. *Neuroimage* 2011;57:167–181.
- (41) Dyrby TB, Baaré WFC, Alexander DC, Jelsing J, Garde E, Sjøgaard LV. An Ex Vivo Imaging Pipeline for Producing High-Quality and High-Resolution Diffusion-Weighted Imaging Datasets. *Hum. Brain Mapp.* 2011;32:544–563.
- (42) Burakiewicz J, Charles-Edwards GD, Goh V, Schaeffter T. Water–fat Separation in Diffusion-Weighted EPI Using an IDEAL Approach with Image Navigator. *Magn. Reson. Med.* 2014, DOI: 10.1002/mrm.25191

## Images

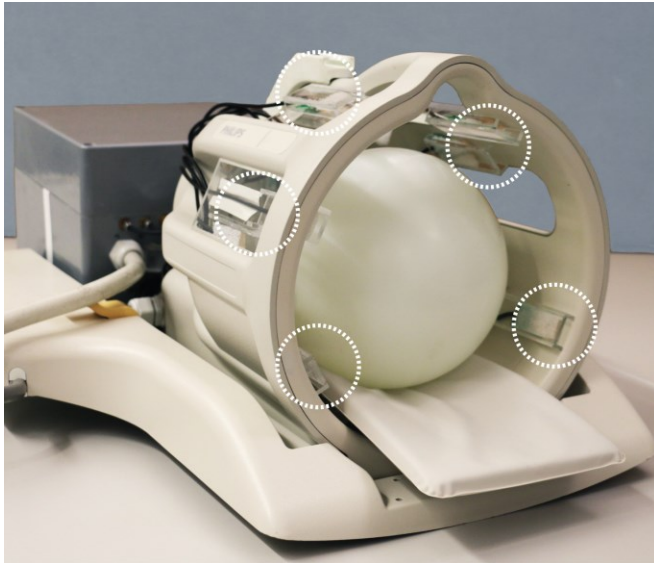


Figure 1: Head-coil array equipped with 16  $^{19}\text{F}$ -based transmit/receive NMR field probes. The dedicated power transmit- and pre-amplification stages for the field probes are housed in the dark grey box in the background.

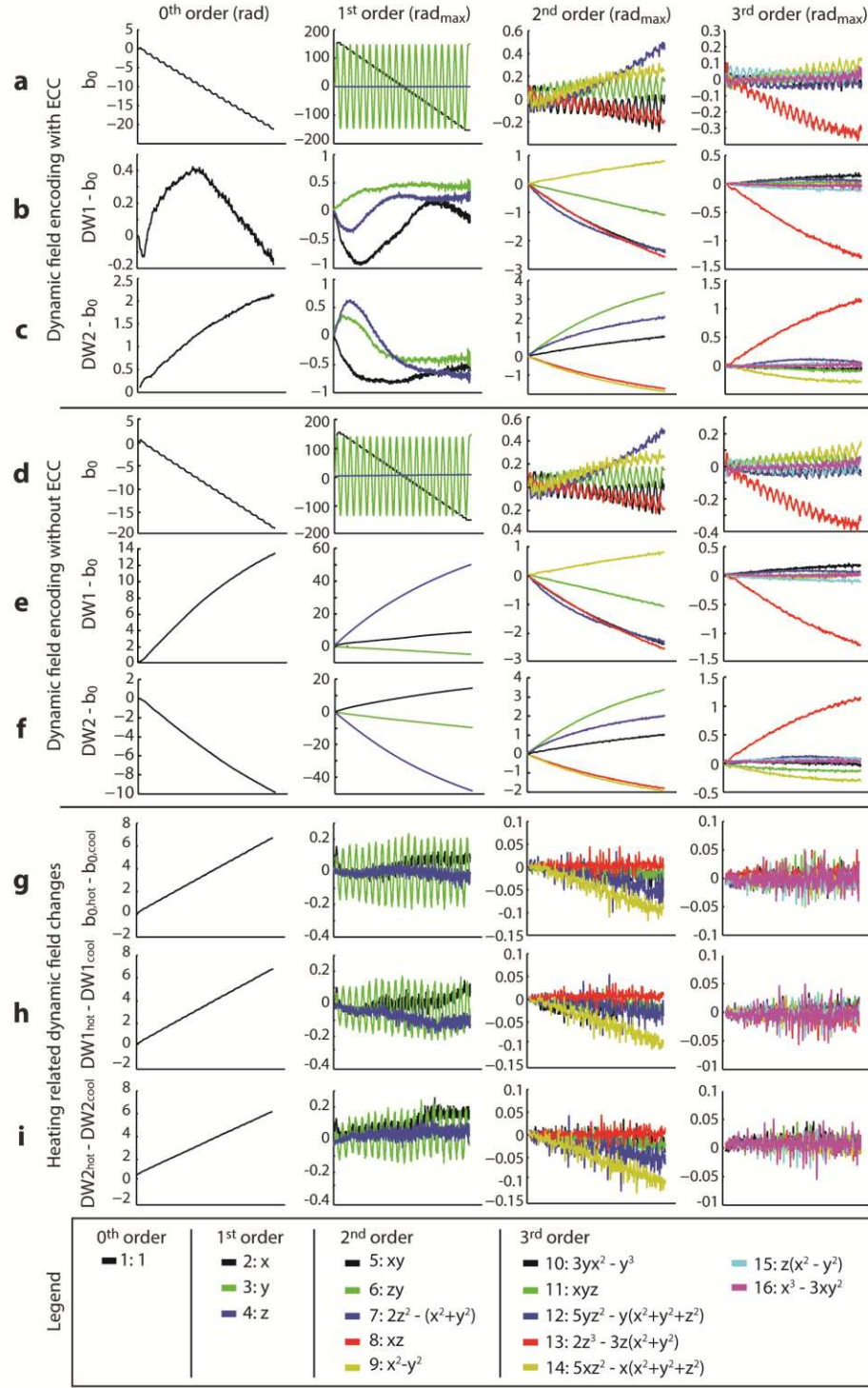


Figure 2: Field evolution during the EPI readout separated by their spatial orders. Scans with (a-c) and without (d-f) ECC. Separated encoding effects of the DW gradients (b,c,e,f). Difference between first (hot) and last (cool) corresponding average (dynamic) of an experiment following a gradient intensive scan plotted for the  $b_0$  (g) and the first two DW acquisitions (h,i). Please note that the y-axis is scaled individually for each plot.



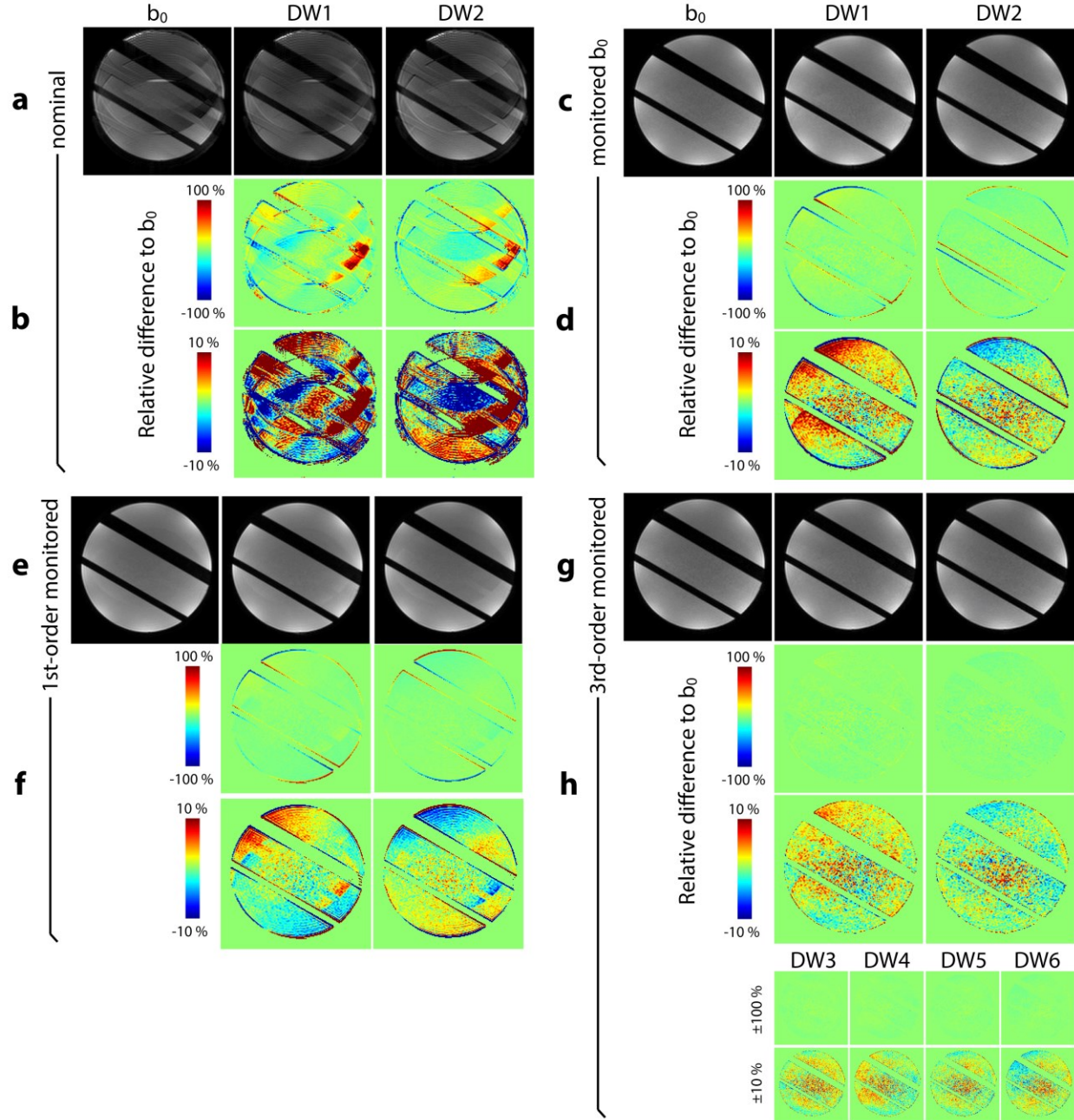


Figure 3: Effect of encoding models on image congruence and ghost level. Images reconstructed with nominal encoding (a) and the differences between DW and corresponding b<sub>0</sub> image (b). Images reconstructed with the monitored 1<sup>st</sup>-order trajectory of the b<sub>0</sub> acquisition (c) and the differences between DW and corresponding b<sub>0</sub> image (d). Images reconstructed using the individually monitored 1<sup>st</sup>-order encoding model (e) and the differences between DW and corresponding b<sub>0</sub> image (f). Images reconstructed using the individually monitored 3<sup>rd</sup>-order encoding (g) and the differences between DW and corresponding b<sub>0</sub> image (h).



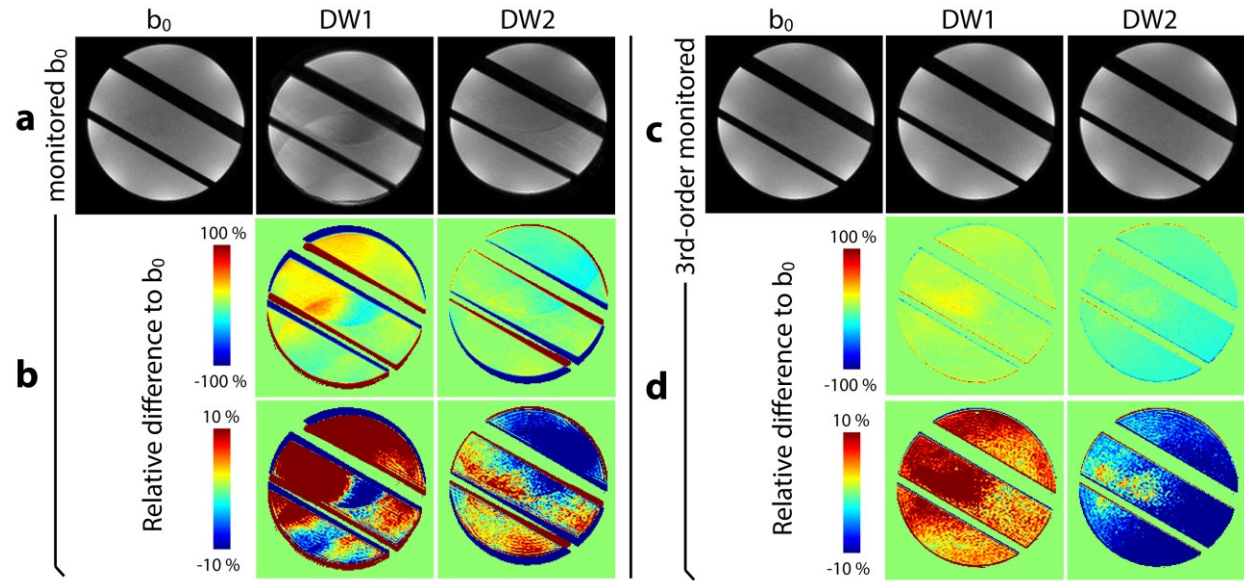


Figure 4: Image congruence without the MR system's ECC with (a) and without (c) concurrent field monitored reconstruction. Differences between DW and corresponding  $b_0$  images (b,d).

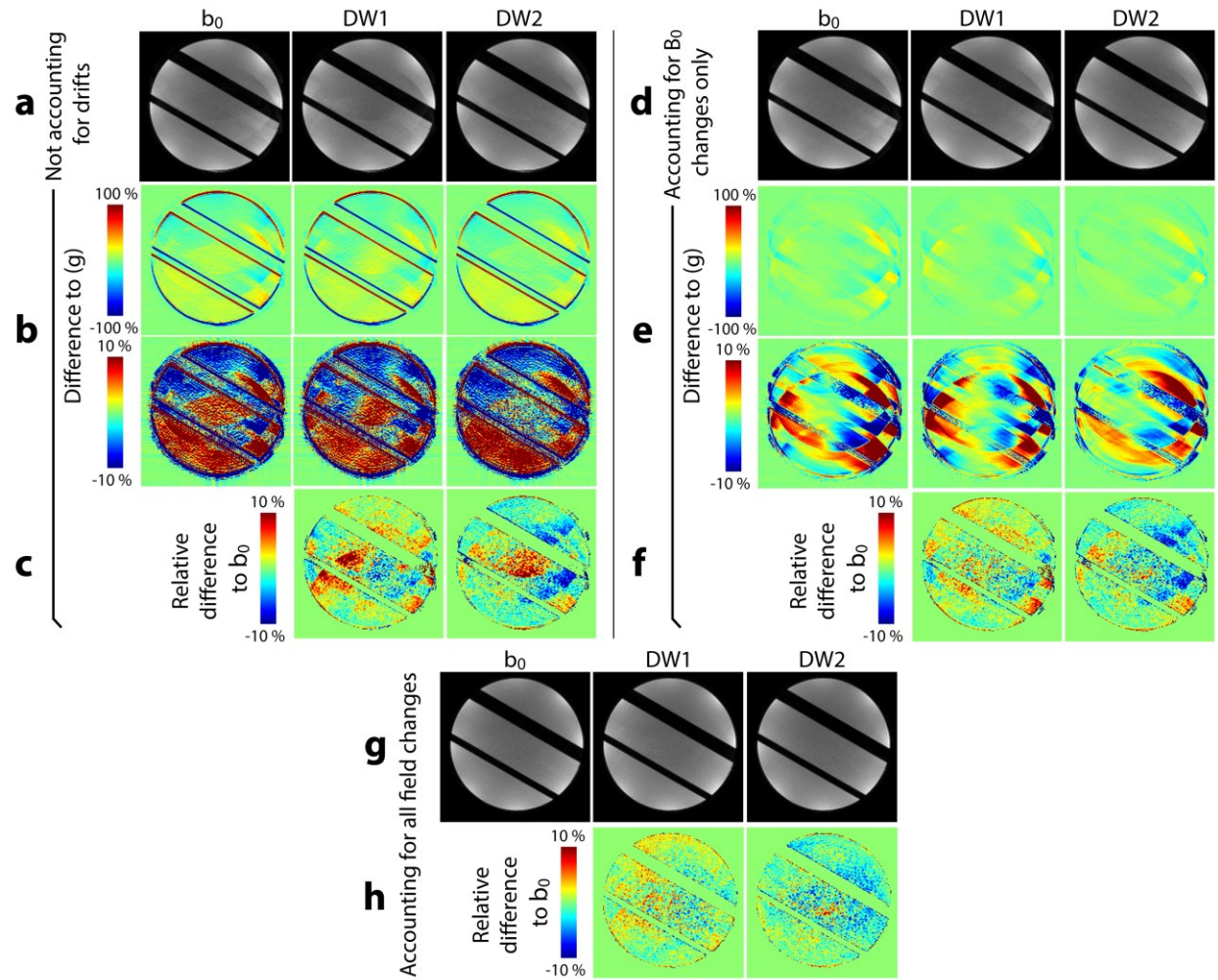


Figure 5: Effect of field/gradient drift during the scan. Images reconstructed when neglecting encoding changes for the individual signal averages (a); differences to the corresponding concurrently monitored images (b); difference to the corresponding  $b_0$  image (c). Images reconstructed when accounting for individual  $B_0$  changes for all signal averages (d; differences to the corresponding concurrently monitored images (e) ; difference to the corresponding  $b_0$  image (f). Images reconstructed when accounting for all concurrently monitored field changes for all signal averages (g); differences to the corresponding  $b_0$  image (h).

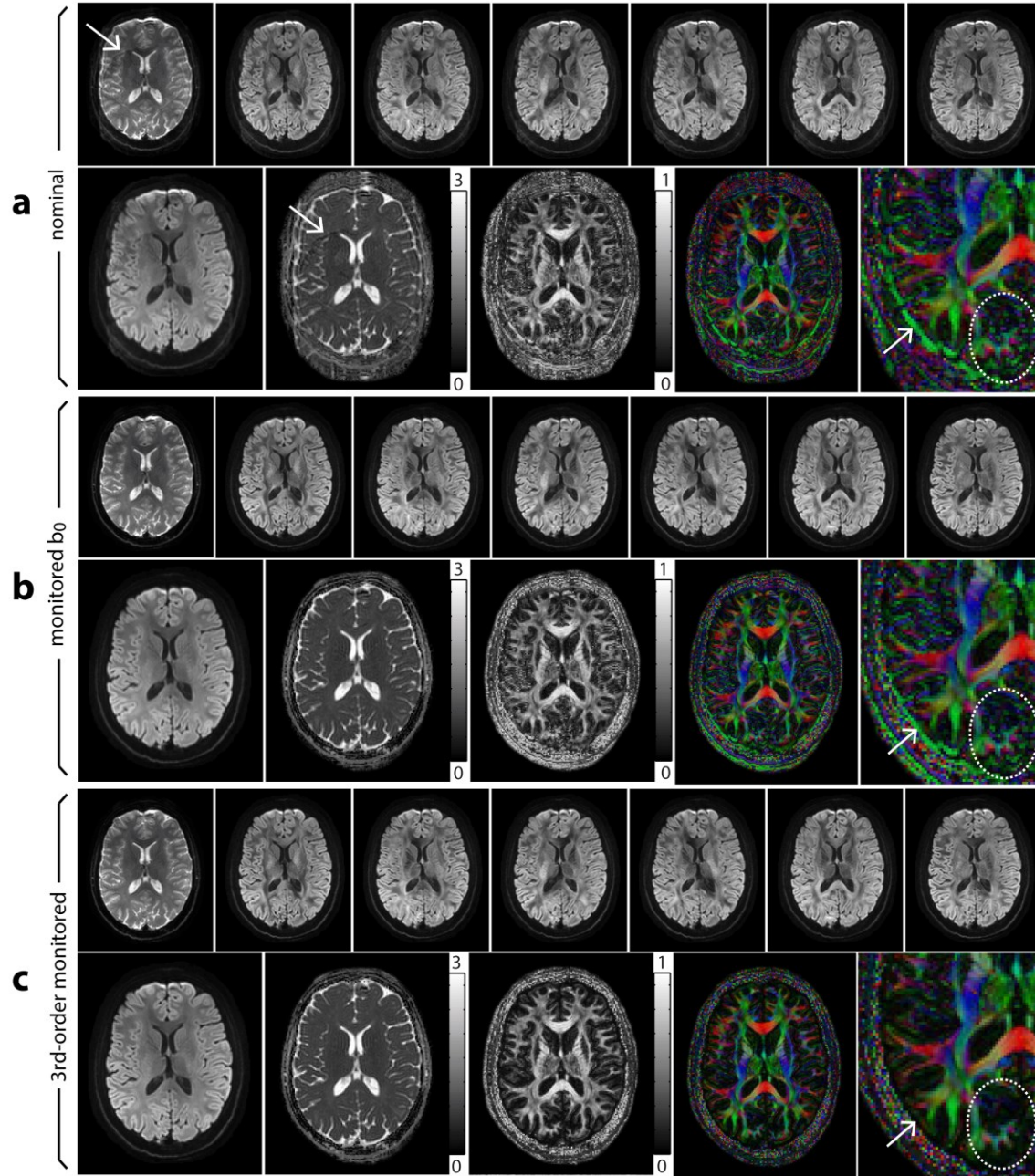


Figure 6: In-vivo DTI data reconstructed on the nominal k-space trajectory (a), the  $b_0$  k-space trajectory (b) and the concurrently monitored 3<sup>rd</sup>-order k-space trajectory (c). Upper row:  $b_0$  (left) and the 6 individual DW directions. Lower row (left to right): mean DW image, ADC map [ $10^{-3}\text{mm}^2/\text{s}$ ], FA map, cFA map, cFA map zoomed. The dashed oval and the arrow in the zoomed color-coded FA (cFA) images highlight noisy and increased FA values and non-physiological anisotropy in (a) and (b).